Solar Chromospheric Temperature Diagnostics: A Joint ALMA-Hα Analysis

Momchil E. Molnar[1,2,5] , Kevin P. Reardon[1] , Yi Chai[3], Dale Gary[3] , Han Uitenbroek[1] , Gianna Cauzzi[1,4] , and Steven R. Cranmer[2]

[1] National Solar Observatory, Boulder, CO 80303, USA; kreardon@nso.edu
[2] Department of Astrophysics and Planetary Sciences, University of Colorado, Boulder, CO 80303, USA
[3] Center for Solar-Terrestrial Research, New Jersey Institute of Technology, Newark, NJ 07102, USA
[4] INAF-Osservatorio Astrofisico di Arcetri, Florence, I-50125, Italy

Abstract

We present the first high-resolution, simultaneous observations of the solar chromosphere in the optical and millimeter wavelength ranges, obtained with the Atacama Large Millimeter Array (ALMA) and the Interferometric Bidimensional Spectrometer at the Dunn Solar Telescope. In this paper we concentrate on the comparison between the brightness temperature observed in ALMA Band 3 (3 mm; 100 GHz) and the core width of the Hα 6563 Å line, previously identified as a possible diagnostic of the chromospheric temperature. We find that in the area of plage, network and fibrils covered by our field of view, the two diagnostics are well correlated, with similar spatial structures observed in both. The strength of the correlation is remarkable, given that the source function of the millimeter radiation obeys local thermodynamic equilibrium, while the Hα line has a source function that deviates significantly from the local Planck function. The observed range of ALMA brightness temperatures is sensibly smaller than the temperature range that was previously invoked to explain the observed width variations in Hα. We employ analysis from forward modeling with the Rybicki-Hummer (RH) code to argue that the strong correlation between Hα width and ALMA brightness temperature is caused by their shared dependence on the population number n_2 of the first excited level of hydrogen. This population number drives millimeter opacity through hydrogen ionization via the Balmer continuum, and Hα width through a curve-of-growth-like opacity effect. Ultimately, the n_2 population is regulated by the enhancement or lack of downward Lyα flux, which coherently shifts the formation height of both diagnostics to regions with different temperature, respectively.

1. Introduction

Analysis of visible, UV, and infrared spectral lines has long provided a key method for extracting information about the solar chromosphere. The lines provide valuable information on velocity, magnetic fields, density stratification, and abundances, among other physical observables. However, due to the low-density conditions under which the chromospheric lines are formed, local thermodynamic equilibrium (LTE) typically does not hold. With an atmosphere whose structuring can be dominated by the local dynamics or the magnetic field topology, there is a possibility of steep gradients in density, temperature, or other parameters along the line of sight. Therefore, the interpretation of the information encoded in chromospheric line profiles is not straightforward. Efforts at inversions of chromospheric spectral lines appear promising (e.g., Socas-Navarro et al. 2015), even though the robust extraction of atmospheric parameters from these profiles is still a subject of much research (Milić & van Noort 2018; de la Cruz Rodríguez et al. 2019).

Previous work has suggested that the bisector width near the core of the Balmer-alpha transition line of hydrogen (Hα from now on) may reveal information about the temperature of the region of the chromosphere where it forms (Cauzzi et al. 2009; Leenaarts et al. 2012). The high temperature sensitivity of Hα width was thought to primarily arise from the low atomic mass of hydrogen, resulting in a significant thermal Doppler broadening. Furthermore, Cauzzi et al. (2009) found strong

correlations between the Hα line width and the width and core intensity of the Ca II 8542 Å line, which they explained with a temperature-dependent microturbulence, and a close coupling with local conditions (temperature), respectively. However, the interpretation of the extreme widths of Hα (reaching 1.2 Å and beyond) in terms of Doppler broadening implied temperatures of up to 50,000 K, which would cause the chromosphere to be fully ionized according to 1D models, and which are rarely found in 3D chromospheric models.

The Atacama Large Millimeter Array (ALMA; Wootten & Thompson 2009), recently made available for solar observations, can provide an observable directly related to the electron temperature of the chromospheric plasma, supposedly freeing us from the non-LTE complications of other diagnostics (Phillips et al. 2015). The continuum radiation at millimeter wavelengths (≈0.3–10 mm) originates from free–free emission in the chromosphere, and the two main opacity sources are the electron-ion free–free absorption and the neutral-electron free–free absorption (away from strong magnetic fields, see Wedemeyer et al. 2016, for further discussion). These processes are coupled solely to the local properties of the plasma (electron temperature) and, therefore, result in an LTE source function. By using the Rayleigh–Jeans law, we can then interpret the emergent intensity in the millimeter wavelength domain as a local electron temperature. This was verified theoretically by Loukitcheva et al. (2015), who showed that, in 3D–MHD models, the ALMA brightness temperature indeed represents the electron temperature at the formation height of the millimeter radiation.
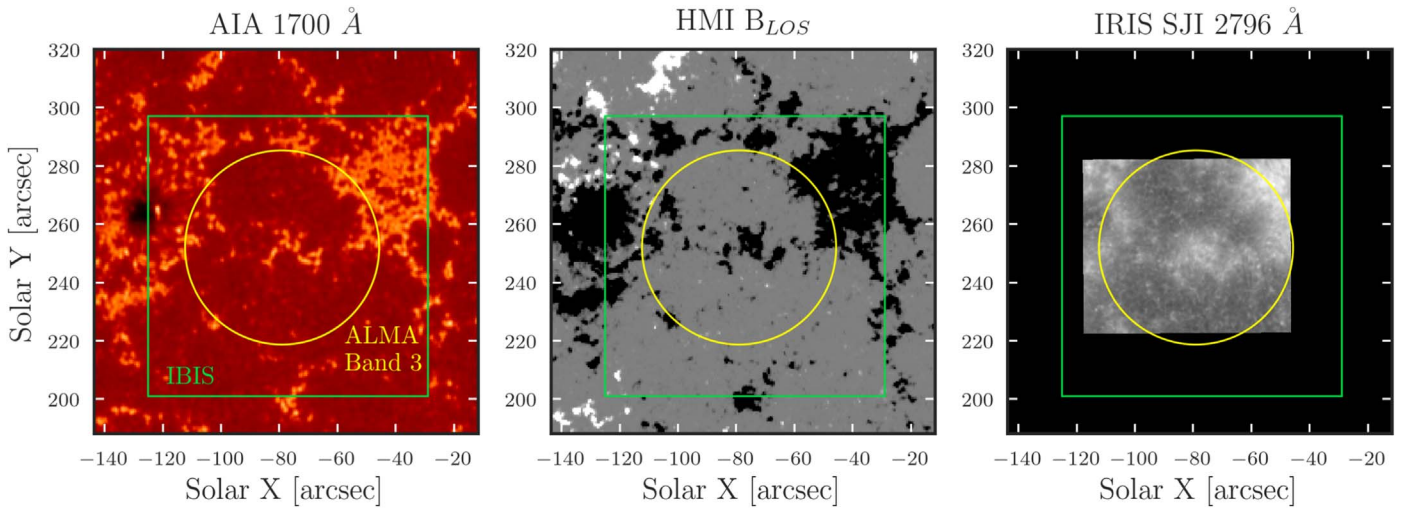
---

[5] DKIST Ambassador.

Figure 1. Context images of the observed field of view (FOV) from the following instruments at 17:25 UT: Left panel: AIA 1700 Å image; central panel: HMI LOS magnetogram, scaled (nonlinearly) between −200 and 200 G.; right panel: *IRIS* SJI image at 2796 Å, averaged over one minute. The FOV of IBIS is shown as the green square and the ALMA Band 3 FOV is shown as the yellow circle.

Early results of solar science with ALMA have been discussed by several authors. Among others, the visibility of chromospheric structures in full-disk ALMA 1.21 mm data has been discussed by Brajša et al. (2018), while the presence and dynamics of chromospheric jets/spicules at the limb is reported by Yokoyama et al. (2018) and Nindos et al. (2018). Using high-resolution *IRIS* observations of the Mg II h line obtained simultaneously, Bastian et al. (2017) showed clearly the difference of temperatures derived from radiative diagnostics (Mg II line intensity) and the plasma temperature derived from ALMA.

In this paper we concentrate on a joint analysis of the intensity measured in the ALMA Band 3 and the Hα line, to further our understanding of the chomospheric temperature structure. To this end, we employ some of the first simultaneous, high-resolution, high-cadence observations of the Sun in the millimetric range and in the optical and near-IR wavelengths.

2. Observations

We obtained a coordinated set of observations between ALMA and the Dunn Solar Telescope (DST, Dunn & Smartt 1991) on 2017 April 23. At the DST, the Interferometric Bidimensional Spectrometer (IBIS, an imaging spectrograph Cavallini 2006; Reardon & Cavallini 2008), the Facility Infrared Spectrograph (a scanning spectrograph, Jaeggli et al. 2010), and the Rapid Oscillations in the Solar Atmosphere instrument (a multichannel broadband imager, Jess et al. 2010) all observed the target region (in the following we concentrate only on the IBIS data). In addition, the *Interface Region Imaging Spectrograph* (*IRIS*: De Pontieu et al. 2014) and *Hinode* (Kosugi et al. 2007) satellites were co-pointing for these observations. Context images were available from *Solar Dynamics Observatory*/Atmospheric Imaging Assembly (*SDO*/AIA; Lemen et al. 2012) and magnetic field maps from *SDO*/Helioseismic Magnetic Imager (HMI; Pesnell et al. 2012).

The observed target, shown in Figure 1, was an area of magnetic plage in the leading portion of NOAA active region 12651, a stable region with low flaring activity present during the declining phase of the solar cycle. Some quieter areas were present in the southern portion of the field of view (FOV). The

center of the target region was at E04, N11 at the time of the observations ($\mu = 0.96$ or heliocentric angle of 16°). The primary leading spot of the active region was located about 60″ east of the target center, outside the FOV of all of the targeted observations.

2.1. DST/IBIS Observations

We observed the target region at the DST from 15:13 to 19:06 UT in conditions of good to excellent seeing. Although several different lines and spectral sampling combinations were obtained within the full observing interval, we focus here on a continuous series of IBIS observations that ran from 17:25 to 18:11 UT, and that included 180 interleaved scans of Hα 6563, Ca II 8542, and Na I D1 5896 Å. The lines were scanned with 29, 27, and 24 spectral sampling points, respectively, requiring between 3.4 and 4.0 s per line. With an additional overhead of 1.5 s to change prefilters, the total cadence for a scan of all three lines was 15.7 s. The spatial scale of the images from IBIS was ∼0″096/pixel.

We applied linearity, dark correction, flatfielding, and fringe removal corrections to the IBIS data. In order to correct for optical and atmospheric image distortions, we employed a technique using the nearest-in-time HMI continuum intensity images in order to precisely map the IBIS spectral data onto a regular, fixed spatial grid with the bulk of the seeing distortions removed.[6]

2.2. ALMA Observations and Processing

The ALMA data were obtained with the array in configuration C40-3 with a maximum baseline of 460 m. However, due to antenna issues, during these observations the maximum baseline was 396 m. The data analyzed here were obtained in Band 3 (2.8–3.3 mm, 92–108 GHz) in the interval 17:19–18:53 UT. The millimetric observations followed a sequence that dwelled for approximately 593 s on the target, followed by a 145 s gap for observations of a phase calibrator. There were eight observing intervals all together, with the final interval

---

6　Using Rob Rutten's very capable software package available at his website: http://www.staff.science.uu.nl/~rutte101/Recipes_IDL.html.

being truncated to 440 s due to the end of the allocated observing block. After applying the standard radio interferometer data calibration procedures using CASA (Petry & CASA Development Team 2012), we found that the ALMA images are heavily influenced by the phase disturbances due to water vapor variations in Earth's atmosphere, causing small-scale distortions on the images. To counteract this effect, we apply a self-calibration technique. For each 10 minute observation interval, an average (clean) image is generated and then used to remove the random phase variations in the individual images within that observing interval. This allows us to minimize the image distortions in a self-consistent manner that does not introduce significant artifacts.

The FOV of ALMA Band 3 images is only $\sim60''$ diameter, which can be smaller than some of the large-scale structuring of solar features. To provide information on the background emission from the Sun, single-dish observations that scan the full disk were taken nearly simultaneously with the interferometer array (White et al. 2017), albeit with a significantly lower spatial resolution. Through the feathering process provided in CASA, we combine the two data sets covering the full range of spatial scales. In order to provide an absolute calibration for the measurements, the full-disk image was normalized such that the brightness temperature in the central region of the disk (diameter $190''$) was equal to 7300 K, as determined by White et al. (2017). This sets the background brightness temperature in our target region. This calibration compensates for any absorption variations in the terrestrial atmosphere and provides an absolute temperature accurate to 2%–5% (White et al. 2017).

Figure 3 (top row) shows examples from the final results after the calibration and feathering procedures. The effective FOV of these Band 3 observations was approximately $60''$ in diameter; the restoring beam size of the ALMA image, as calculated in CLEAN, is $1''\!.75 \times 1''\!.91$ in the x–y directions. The shape of the synthesized beam depends on the antenna configuration and the angle between the array and the target, which means it is not circularly symmetric. While the beam size will change size and shape slightly over time, our observing interval was short enough that there were no significant changes to the beam shape.

3. Diagnostics Comparison

3.1. IBIS Linewidths

We concentrated on the diagnostics afforded by the Hα line, calculating several parameters from the spectral profiles recorded at each pixel and for each time step. The intensity and wavelength of the line-minimum position were determined through fitting of a second-order polynomial to the line core. We calculated the width of the line core following the technique described in Cauzzi et al. (2009)—in short, we measure the separation of the line profile wings at half of the line depth, defined as the difference between the line minimum and the intensity at ±1.0 Å from the core position. This determines the line width in the central core of the line profile, which is essentially the portion formed at chromospheric heights. The instrumental profile has a negligible effect on the measured width, and the errors in the line width were determined to be about 0.005 Å.

Intensity and line width maps for the data acquired at 17:25 UT are shown in Figure 2. While the Hα core intensity

shows the familiar "forest" of chromospheric fibrils originating from magnetic features and covering much of the internetwork regions (compare Figure 1), the line width map shows a significantly different scene. The plage and magnetic network are clearly highlighted as regions of large linewidths, together with the base and partial length of a selected set of fibrils, as discussed in Cauzzi et al. (2009). There is fine spatial structuring in the line width, down to the resolution limit of the data.

3.2. ALMA Band 3 Intensity

The ALMA Band 3 intensity maps are shown in the top row of Figure 3. As stated above, the resolution of the ALMA images is $\approx2''\!.0$.

The top left panel in Figure 3 displays a single 2 s ALMA integration, whereas the top right panel is a time average over the 10 minute time block observed between 17:31 UT and 17:41 UT.

From the similarity of the instantaneous and time-averaged maps, it appears that at this spatial resolution the structures remain fairly stable over several minutes, although ALMA movies show subtle evolution; a complete temporal analysis is left for a future work.

The 3 mm intensity maps are clearly brighter (hotter) in network and plage regions, with T_B reaching up to $\sim12,000$ K in the latter, whereas in the internetwork temperatures are as low as ~6500 K. The overall average T_B for our field is ~8600 K, reflecting the presence of plage in the FOV; the average in the quieter portions of the FOV is ~7500 K. This is consistent with the quiet Sun calibration described in Section 2.2.

The most interesting property of the ALMA T_B maps, however, might be the presence of several bright ALMA features that appear fibrilar in nature, reminiscent of those observed in the Hα line width map of Figure 2. They are particularly prominent in the bottom part of the FOV, where some of the strongest Hα-width features are seen. To the best of our knowledge, this is the first time that fibrilar structures are clearly identified in on-disk ALMA images. Contrary to the prediction of Rutten (2017), however, we identify them as bright (hence hot) features, rather than dark, strong fibrils coincident with Hα line-core intensity features.

3.3. Comparison between the ALMA Band 3 Intensity and Hα Line Width

The bottom panels of Figure 3 show the maps of Hα width acquired cotemporally to the ALMA maps: a single snapshot in the left column, and the average over the period 17:31–17:41 UT in the right column. Contours of the HMI longitudinal magnetic field magnitude at values of greater than 500 Gauss have been drawn in yellow on the right panel to facilitate comparison with Figure 1. In order to provide a more relevant comparison, we have degraded the spatial resolution of the IBIS data to best match the appearance of the ALMA data. We find that the minimum difference between the blurred Hα width and ALMA images occurs for a circular Gaussian with an FWHM $2''\!.0$. This is about 8% greater than the mean FWHM of the theoretical ALMA beam, likely due to residual atmospheric smearing at the millimeter wavelengths. Since the ALMA point-spread function is known to be non-circular due to the orientation of the interferometer array with respect to the object, we apply the ratio between the x and y axes of the
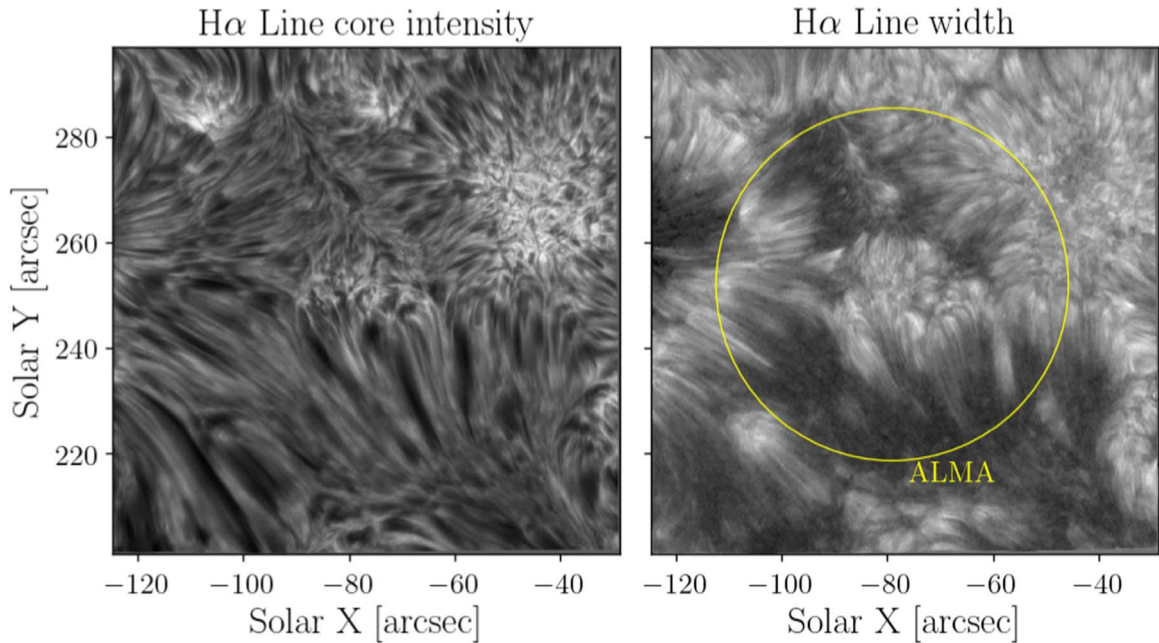
Figure 2. Left panel: Hα core intensity of the region observed by IBIS at 17:25 UT; right panel: Hα line core width, scaled from 0.95 to 1.3 Å, with brighter pixels corresponding to relatively broader profiles. The yellow circle shows the approximate ALMA FOV (see text for more details).

ALMA beam (as calculated for our observations by CLEAN) and convolve the IBIS images with an elliptical Gaussian kernel having FWHM in the x–y directions of $1\rlap{.}''95 \times 2\rlap{.}''03$, respectively. In fact, the match is so satisfactory that we were able to align the Hα width maps and ALMA images to easily achieve subarcsecond accuracy. The alignment between the two diagnostics was done on the time-averaged images and, given the spatial resolution, did not appear to produce any artificial superposition of localized features. Because the temporal sampling was higher for ALMA compared to the multiline IBIS scans (2 versus 15 s), we temporally binned the ALMA data to match the IBIS temporal sampling by combining the eight closest-in-time ALMA brightness maps.

The similarity between ALMA intensity and Hα width is striking, with regions of similar size, shape and contrast. High/low brightness temperature in ALMA Band 3 correspond, almost one-to-one, to broad/narrow Hα profiles. The HMI contours make clear how the ALMA fibrilar structures represent the lower portion of heated features originating from regions with high magnetic flux, like those seen in Hα.

To quantify the comparison, a 2D histogram between the temporally coincident maps of ALMA Band 3 brightness temperature and Hα width is shown in Figure 4. The histogram derived from the overall time average of these two diagnostics shows an essentially identical distribution. The correlation is very strong across the full range in temperature present in our FOV, with a Pearson correlation coefficient of 0.84. Because of the scatter present in both measurements, we perform an orthogonal distance regression (Isobe et al. 1990) to find the best linear fit between the two parameters. The best-fit equation is $0.553 + (6.12e \times 10^{-5})T_{ALMA}$, which is plotted in Figure 4.

However, the range of T_B measured with ALMA is not large enough to explain the change of the observed Hα line width from 0.95 to 1.2 Å as solely due to thermal Doppler broadening, as hypothesized by Cauzzi et al. (2009). This is because the Hα line width already has a significant intrinsic width of around 0.95 Å and this dominates the quadratic sum of broadening components for the observed range of ALMA temperatures. In fact, an increase from 6000 to 12,000 K (Figure 3 top row) would only be expected to increase the line width by 0.025 Å, an order of magnitude smaller than the observed broadening.

Finally, we note the presence of a cluster of points between 6500 and 7500 K for which the Hα widths fall 0.03–0.05 Å lower than the fitted correlation. These points correspond to quieter regions in the bottom half of the ALMA FOV, and located farther away from the magnetic concentrations.

4. Synthetic Spectral Diagnostics with RH

To investigate the mechanisms behind the correlation of Figure 4, we utilized the RH code (Uitenbroek 2001) to synthesize observables for different solar atmospheric models. We chose the 1D Solar Radiation Physical Modeling (SRPM from now on) models (Fontenla et al. 2011) as inputs for our work. We used models ranging from the quiet sun internetwork (model B) to bright facular region (model P), representative of the different solar structures in our FOV. We also included the heritage quiet sun VAL C model for comparison (Vernazza et al. 1981). The RH calculations were done using a 4-level (including continuum) hydrogen atom with the Lyα, Lyβ, and Balmer-alpha transitions treated under partial redistribution, while the rest of the atomic species were treated in LTE. The widths of the chromospheric core of the synthetic Hα profiles were measured using the same method used for the observational data. The emergent millimetric radiation was calculated from the synthetic intensity under the Rayleigh–Jeans approximation for a wavelength range of 2.6–3.4 mm (115–88 GHz), which covers the observed wavelength interval.

The SRPM models have shortcomings, as they are 1D, hydrostatic, semiempirical models optimized to reproduce the temporally averaged solar spectrum as observed at a few arcseconds resolution. Yet, given that the data of Figure 4 have been smoothed to a similar resolution, we use them as a first attempt to provide some physical insight. It is also worth noticing that modern, ab initio 3D–MHD atmospheric models such as
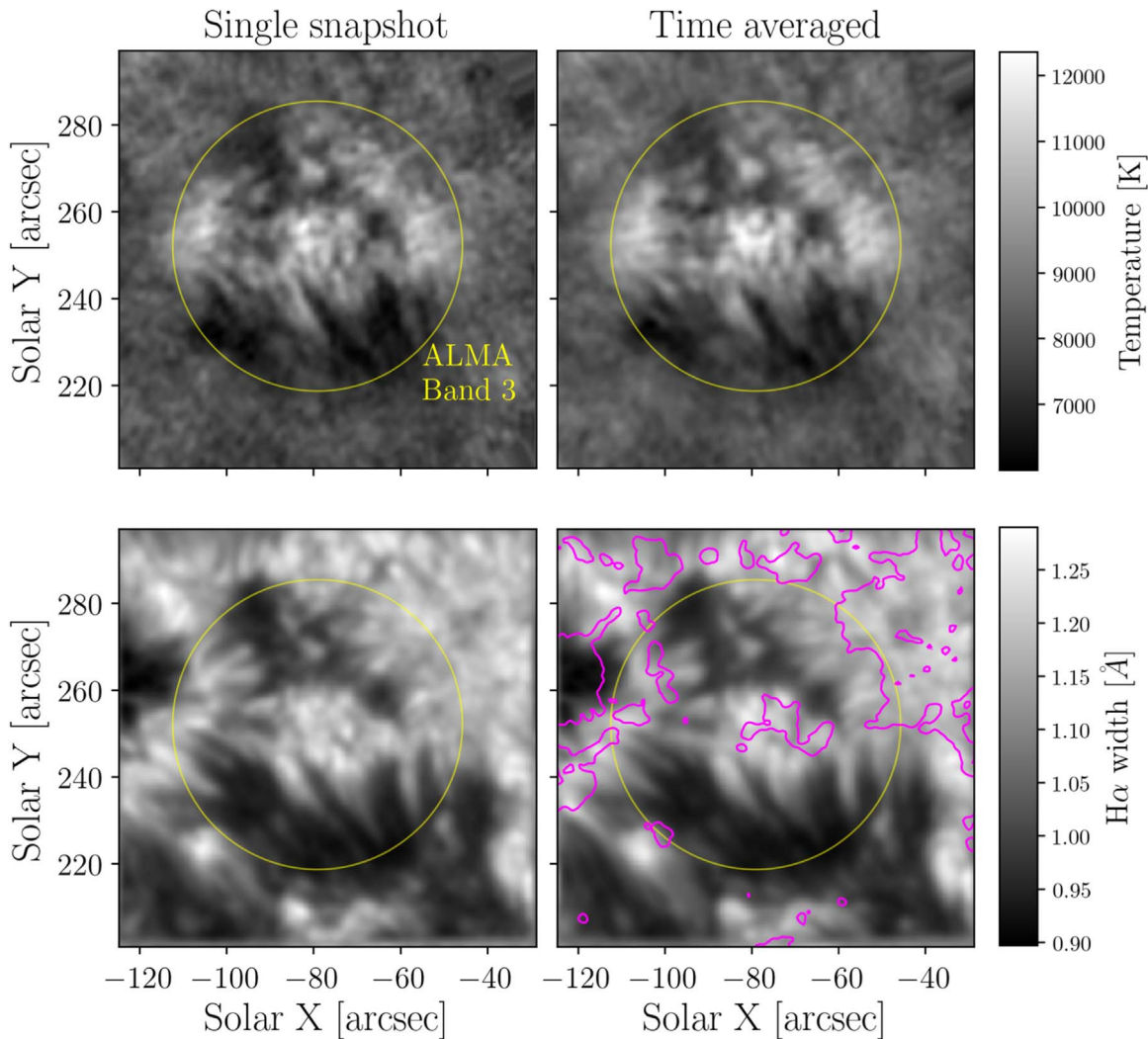
Figure 3. Maps of ALMA intensity (top row) and IBIS Hα line width (bottom row). The left column shows the two parameters at single time step of the observations, while the right column shows the same two parameters averaged over the ten minutes of a continuous ALMA observation block. The IBIS data have been smoothed to match the resolution of the ALMA data, by using a elliptical Gaussian kernel with FWHM in the x–y directions of $1''95 \times 2''03$. The yellow circle with a diameter of $66''$, is slightly larger than the usable FOV of ALMA. The purple contours overlaid on the bottom right panel show areas with magnetic field strength above 500 Gauss, measured by HMI.

BIFROST (Gudiksen et al. 2011; Carlsson et al. 2016) still lack some significant physical processes in the range of heights of relevance for our work; in particular, they do not reproduce the correct width of chromospheric lines (Leenaarts et al. 2009), which is obviously crucial for our analysis. In addition, it would be more correct to perform the radiative transfer calculations for Hα using full, 3D radiative transfer computations (Leenaarts & Carlsson 2009), but we leave that to future work, due to complexity and computational requirements.

The results from the RH line synthesis are presented in Figure 4 as blue circles, and coincide well with the observational data for models B to P, which are the dominant features in our observations (note that hotter models, e.g., model Q, do not follow the trend shown in Figure 4, hinting at a perhaps different behavior for other solar features like active regions). The VAL C result falls below the observed correlation, with too small of a line width, likely due to some of the simplified physical assumptions in that older model (e.g., lack of ambipolar diffusion and a different treatment of Lyα). The range of ALMA temperatures reproduced by the models is not surprising, since the semiempirical models were tailored to reproduce observed millimeter

continuum brightness, among other diagnostics. The observed range of temperatures and correspondence to the appropriate chromospheric structures in the field confirms the proper calibration of the ALMA brightness temperature and consistency with previous work. However, the SRPM models were not constructed using Hα linewidths as a parameter, which makes the close correspondence especially pleasing.

Using the RH results, we can investigate the formation of Hα and the millimetric radiation in more detail. Figure 5 shows the run of relevant parameters for different atmospheric models. In the top left panel, we see how the Hα line saturates even in the colder models, and grows broader as the chromospheric temperature rises. Interestingly, this appears directly correlated with sensibly higher populations of the hydrogen $n = 2$ level in the hotter models, as plotted in the top right panel. Indeed, the number density of H atoms in the $n = 2$ level increases by two orders of magnitude from model B to model P, suggesting that the broadening of Hα could be primarily due to an opacity effect (akin to a curve-of-growth plot).

The middle and bottom panels of Figure 5 show the intensity contribution functions for both diagnostics, for the representative
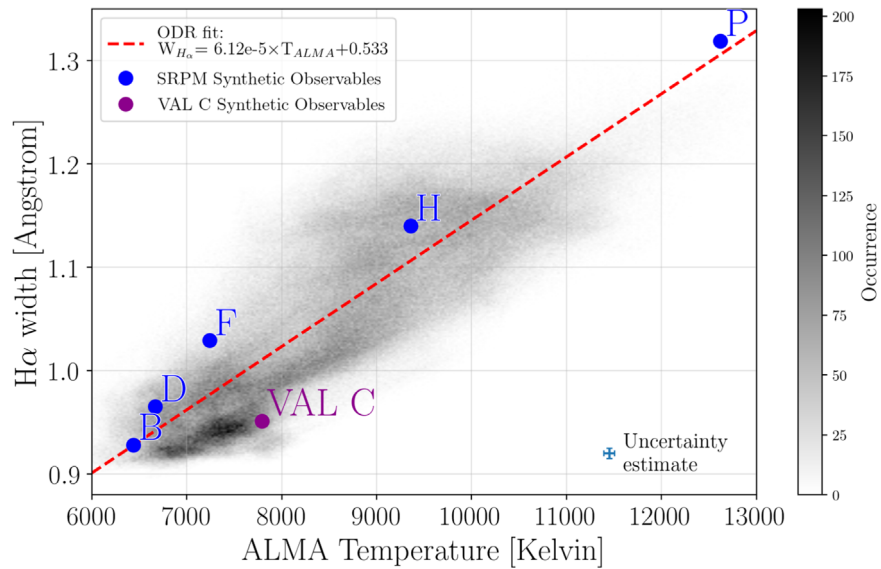
Figure 4. 2D histogram of Hα core width vs. ALMA brightness temperature, clearly showing the correlation between the two quantities. Overlaid as blue dots are the results from the RH spectral synthesis in the Solar Radiation Physical Modeling (SRPM) atmospheres and in violet in the VAL C model. The uncertainty estimates in both directions are presented with the marker in the bottom right of the plot. The spread in the figure is physical, as it is significantly larger than the uncertainties in our measurements. Orthogonal distance regression (ODR) was used to fit the observation with a straight line, resulting in the red dashed line.

models D and H. The emergent intensities over both the Hα profile and the ALMA Band 3 wavelengths are plotted in violet (in the left panels we also show the width of the resulting Hα line, as computed with our method marked with the red line). These panels show that while both diagnostics form over the same general expanse of the chromosphere, their range of formation becomes narrower and more coincident as we move to hotter models. This is represented in the top right panel, where the symbols indicate the heights at which the optical depth $\tau = 1$ for the 3 mm radiation (triangles) and for Hα line core (circles).

For model H, a large fraction of the Hα core intensity, and essentially all of the millimetric intensity originates from a narrow region at the interface of the chromosphere and the transition zone. For the colder model atmospheres, the height separation between the two diagnostics becomes significant. However, some correlation between the diagnostics is still to be expected because both temperature and the hydrogen $n = 2$ level populations (see below) vary very slowly in the relevant range of heights.

We hypothesize that the underlying physical mechanism for the correlation shown in Figure 4 could arise from the common sensitivities of both diagnostics to the population numbers in the first excited state of hydrogen, n_2, in particular as related to excitation in Lyα. Most excitations in Lyα occur via radiative transitions, as not many electrons have sufficient energy to collisionally excite the line at chromospheric temperatures. Opacity in the line core is very high and the radiation field is completely thermalized. However, there is significant excitation in the line wings by radiation coming from the hot transition region above (Uitenbroek 2003; Leenaarts et al. 2012). Being this far in the UV, the additional radiative excitation through downward flux of Lyα wing photons is very sensitive to the column mass at which the transition region occurs. In Figure 5 (upper right) the effect of the downward radiation in the Lyα wings is visible as the bump on the right side of the n_2 level population plot, on top of the general rise from one model to the next that is caused by the increase in density scale height associated with hotter models.

On the one hand, an enhanced value of n_2 leads to enhanced ionization of hydrogen, as the predominant mechanism for hydrogen ionization in the chromosphere is via the Balmer continuum, which decouples from local conditions already much deeper in the atmosphere (Carlsson & Stein 2002). Since the radiation field in the Balmer continuum is optically thin, any fractional increase in the $n = 2$ populations will raise ionization levels proportionally. The increase in electrons coming from this increase in $n = 2$ population raises the opacity at 3 mm, moving the formation height of radiation at these wavelengths up in the atmosphere to higher temperatures; this results in raising the millimetric brightness temperature, once hydrogen ionization reaches a few percent.

On the other hand, an increase in n_2 raises the opacity in Hα, also increasing the formation height of the core in particular. The line source function of Hα is almost flat with height through the chromosphere, resulting in the characteristic flat bottom of the line profile in the core. Changing wavelength from the core outward in the line profile, the intensity follows the flat source function inward (Leenaarts et al. 2012; Rutten & Uitenbroek 2012), until it suddenly becomes sensitive to the photospheric temperature rise with depth, resulting in the steep wings of the line profile. The further the line core formation moves up in the atmosphere, the further in wavelength we have to move out of the core to see the wings, explaining the dependency of the Hα width as an opacity effect, rather than a direct effect from thermal broadening.

Thus, we suggest that both the 3 mm brightness temperature and the Hα line width depend coherently on the n_2 level populations of hydrogen in the chromosphere. With higher values of n_2 the formation height of the 3 mm radiation increases through increased hydrogen ionization in the Balmer continuum as explained above. At the same time, an increase in n_2 leads to opacity broadening of Hα through an upward shift of the core formation height (as noted above, for the hotter SPRM Q the trend breaks down as Hα forms at the base of the TR where the higher source function leads to an increased line core intensity), and the effect of an almost flat source function
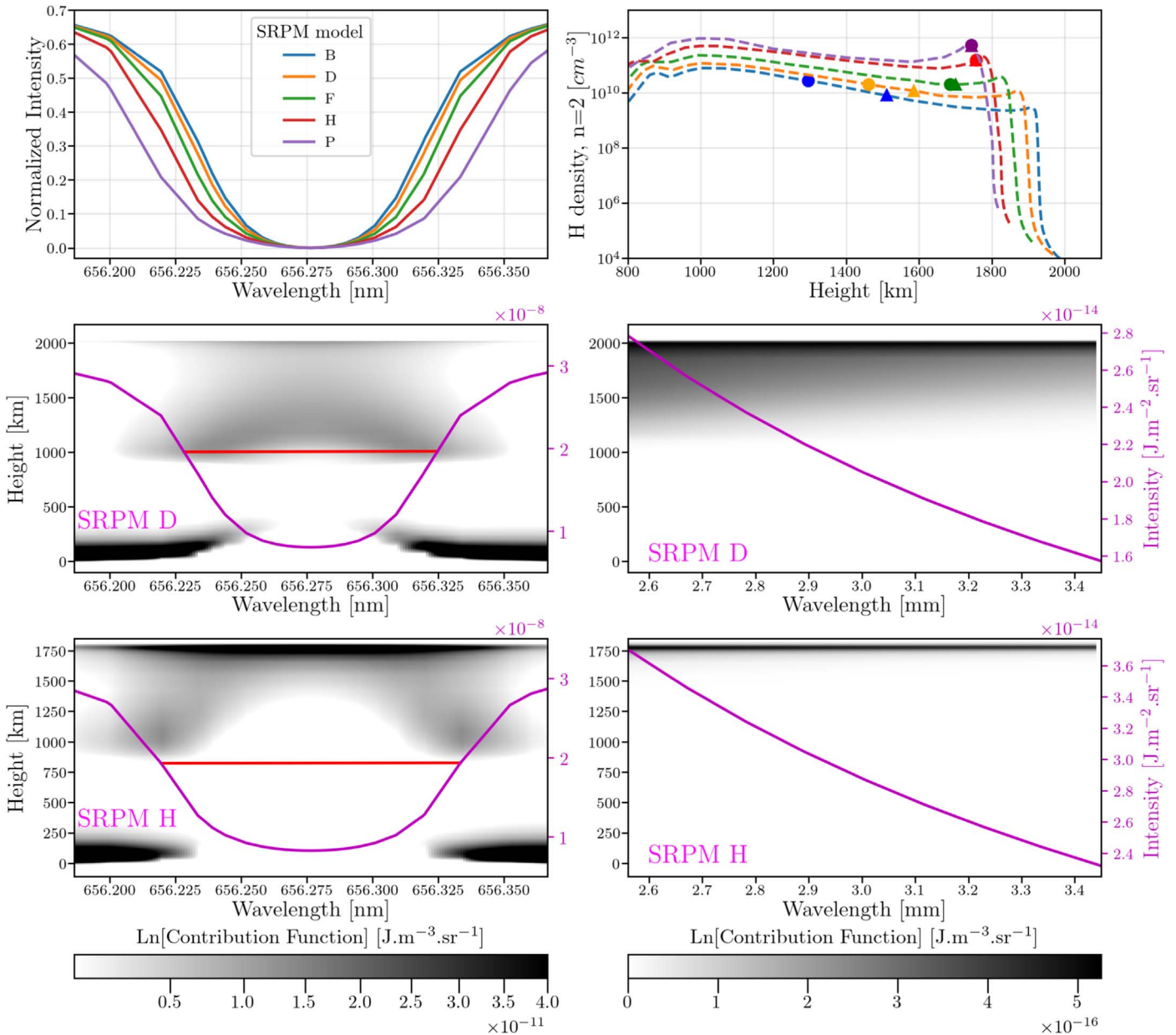
Figure 5. Results from the RH spectral synthesis. Upper left: Hα profiles for the different SRPM atmospheres. Upper right: number density of hydrogen atoms in the $n = 2$ quantum state. The symbols show the height at which $\tau = 1$ for the 3 mm radiation (triangles) and the Hα line core intensity (circles), in the corresponding atmosphere. Note that the triangles and circles indicating the $\tau = 1$ surfaces coincide for the hotter models. Middle left: intensity contribution function for the Hα line for the SRPM D model overlaid with the emergent line profile (in violet). Note the different intensity scaling with respect to the upper panel. The position of the line width measurement described in Section 3.1 is illustrated with the red line. Middle right: contribution function for the emergent intensity for ALMA Band 3 wavelengths for the SRPM D model, overlaid with the emergent intensity profile (in violet). Bottom left, right: as the middle panels, for the SRPM H model.

of the line through the chromosphere. The n_2 population of hydrogen in the chromosphere is determined by the downward Lyα wing flux (Carlsson & Stein 2002), and, in turn, the Lyα flux is determined by the column mass at which the TR occurs (Mariska 1992). Indeed, in our synthesis we found increasing Lyα flux for the hotter models (B to P), whose TR location occurs at increasing column mass. This is in agreement with our conjecture about the correlation between Hα width and ALMA brightness temperature.

5. Conclusions

We have presented the first observations combining high-spatial-resolution spectral imaging in the traditional chromospheric

indicator of Hα, combined with simultaneous brightness temperature maps at millimeter wavelengths obtained with ALMA. The common ∼60″ diameter FOV of the two instruments contained plage, network, and some (magnetically) quieter areas.

The ALMA 3 mm images display a structured pattern of bright (hotter) and dark (cooler) features, with spatial sizes down to the spatial resolution of ∼2″.0. The corresponding brightness temperature spans a range between 6500 and 12,000 K. An interesting property of the ALMA T_B maps is the presence of bright ALMA features that appear fibrilar in nature, particularly prominent in the bottom part of the FOV. The ALMA images bear a striking similarity with the maps of the Hα line core width, with features of similar size, shape, and contrast (Figure 3). This is contrary to the predictions presented

in a recent paper by Rutten (2017), that hypothesized the ubiquitous presence of long, opaque ALMA fibrils, with a good dark–dark correspondence with the Hα core intensity; as shown also in Cauzzi et al. (2009), the Hα core intensity and width are poorly correlated quantities. We however defer a more detailed comparison of such features to a further work.

Our most important result is the strong quantitative correlation between the intensity of ALMA and the width of the Hα line core in the range of observed temperatures, as plotted in Figure 4. Using forward synthesis with RH, we showed that the correlation is well reproduced with 1D semiempirical models of typical solar structures, which further indicates that the Hα intensity and the millimeter radiation are formed in a similar span of the middle-upper chromosphere. We note that the synthesis from the VAL C model falls below the observed correlation and away from the other modeling results, most likely due to the inclusion in the SRPM models of ambipolar diffusion and a different, more detailed treatment of the Lyα line profile.

The main factor driving the correlation appears to be that the opacity sources for both spectral diagnostics is determined through the $n = 2$ hydrogen population. The mm-wavelength opacity depends on the electron number density, which is related to the $n = 2$ population of hydrogen as the statistically dominant source of free electrons in the upper chromosphere. At the same time, the line-broadening of Hα is determined by the column mass of $n = 2$ hydrogen atoms in a manner similar to a curve-of-growth effect. This effect is stronger in hotter atmospheric models, for which the height of formation of both diagnostics coincides almost exactly as it is pushed to the chromosphere-TR boundary. The direct contribution to the Hα line width from solely thermal Doppler broadening for the range of temperatures detected with ALMA (between 6500 K to 12,000 K) is only about 0.025 Å, an order of magnitude smaller than the observed variation of 0.3 Å.

Indeed, the earlier interpretation of Hα width as due essentially to thermal broadening (Cauzzi et al. 2009) required a much larger range of electronic temperatures, all the way to $T_e \sim 60{,}000$ K. With the reliable determination of T_e now provided by ALMA, it appears necessary to revisit the original assumption of negligible changes due to radiative transfer effects (essentially contained in the "intrinsic" width of the lines in Cauzzi et al. 2009), at least for Hα. A strong correlation between Hα width and Ca II 8542 width and core intensity has also been observed in the data set discussed in this paper, and will be the subject of a future investigation. We note that the smaller temperature range found here to explain the Hα line width does not alter the need for a temperature-dependent microturbulent broadening to produce the observed distribution of widths of the Ca II 8542 line.

Of more general utility, we have demonstrated that the Hα line width can be as useful and meaningful of an indicator of the temperature of the chromosphere and the initial rise into the transition region as those temperatures derived from ALMA millimeter intensities, at least in the range 6500–12,000 K. While it too suffers from the same changes in the heights of formation as the millimeter radiation, given the above caveats it can represent an easily accessible and straightforward diagnostic of chromospheric temperatures in many regions of the chromosphere. The combination of Hα line width and ALMA 3 mm observations has in effect allowed us to calibrate the linewidths in terms of brightness temperature (for observations

of network regions and near disk center). Future work should examine the nature of the relationship at different heliocentric angles or for different structures. The values of the linear fit can be used to derive an approximate conversion of the line width to chromospheric 3 mm brightness temperature with an accuracy of better than 1000 K. Given the good matching between the 1D models and the Hα line width, the measured value could provide an efficient method to make better initial guesses of the input atmosphere for spectral inversions of chromospheric lines.

ORCID iDs

Momchil E. Molnar ⓘ https://orcid.org/0000-0003-0583-0516
Kevin P. Reardon ⓘ https://orcid.org/0000-0001-8016-0001
Dale Gary ⓘ https://orcid.org/0000-0003-2520-8396
Han Uitenbroek ⓘ https://orcid.org/0000-0002-2554-1351
Gianna Cauzzi ⓘ https://orcid.org/0000-0002-6116-7301
Steven R. Cranmer ⓘ https://orcid.org/0000-0002-3699-3134

References

Bastian, T. S., Chintzoglou, G., De Pontieu, B., et al. 2017, ApJL, 845, L19
Brajša, R., Sudar, D., Benz, A. O., et al. 2018, A&A, 613, A17
Carlsson, M., Hansteen, V. H., Gudiksen, B. V., Leenaarts, J., & De Pontieu, B. 2016, A&A, 585, A4
Carlsson, M., & Stein, R. F. 2002, ApJ, 572, 626
Cauzzi, G., Reardon, K., Rutten, R. J., Tritschler, A., & Uitenbroek, H. 2009, A&A, 503, 577
Cavallini, F. 2006, SoPh, 236, 415
de la Cruz Rodríguez, J., Leenaarts, J., Danilovic, S., & Uitenbroek, H. 2019, A&A, 623, A74
De Pontieu, B., Title, A. M., Lemen, J. R., et al. 2014, SoPh, 289, 2733
Dunn, R. B., & Smartt, R. N. 1991, AdSpR, 11, 139
Fontenla, J. M., Harder, J., Livingston, W., Snow, M., & Woods, T. 2011, JGRD, 116, D20108

Gudiksen, B. V., Carlsson, M., Hansteen, V. H., et al. 2011, A&A, 531, A154
Hunter, J. D. 2007, CSE, 9, 90
Isobe, T., Feigelson, E. D., Akritas, M. G., & Babu, G. J. 1990, ApJ, 364, 104
Jaeggli, S. A., Lin, H., Mickey, D. L., et al. 2010, MmSAI, 81, 763
Jess, D. B., Mathioudakis, M., Christian, D. J., et al. 2010, SoPh, 261, 363
Kosugi, T., Matsuzaki, K., Sakao, T., et al. 2007, SoPh, 243, 3
Leenaarts, J., & Carlsson, M. 2009, in ASP Conf. Ser. 415, The Second Hinode Science Meeting: Beyond Discovery-Toward Understanding, ed. B. Lites et al. (San Francisco, CA: ASP), 87
Leenaarts, J., Carlsson, M., Hansteen, V., & Rouppe van der Voort, L. 2009, ApJL, 694, L128
Leenaarts, J., Carlsson, M., & Rouppe van der Voort, L. 2012, ApJ, 749, 136
Lemen, J. R., Title, A. M., Akin, D. J., et al. 2012, SoPh, 275, 17
Loukitcheva, M., Solanki, S. K., Carlsson, M., & White, S. M. 2015, A&A, 575, A15
Mariska, J. T. 1992, The Solar Transition Region (Cambridge: Cambridge Univ. Press)
Milić, I., & van Noort, M. 2018, A&A, 617, A24
Nindos, A., Alissandrakis, C. E., Bastian, T. S., et al. 2018, A&A, 619, L6
Oliphant, T. 2006, NumPy: A Guide to NumPy (Trelgol Publishing)
Pesnell, W. D., Thompson, B. J., & Chamberlin, P. C. 2012, SoPh, 275, 3
Petry, D. & CASA Development Team 2012, in ASP Conf. Ser. 461, Astronomical Data Analysis Software and Systems XXI, ed. P. Ballester, D. Egret, & N. P. F. Lorente (San Francisco, CA: ASP), 849
Phillips, N., Hills, R., Bastian, T., et al. 2015, in ASP Conf. Ser. 499, Revolution in Astronomy with ALMA: The Third Year, ed. D. Iono et al. (San Francisco, CA: ASP), 347
Reardon, K. P., & Cavallini, F. 2008, A&A, 481, 897
Rutten, R. J. 2017, A&A, 598, A89
Rutten, R. J., & Uitenbroek, H. 2012, A&A, 540, A86
Socas-Navarro, H., de la Cruz Rodríguez, J., Asensio Ramos, A., Trujillo Bueno, J., & Ruiz Cobo, B. 2015, A&A, 577, A7
Uitenbroek, H. 2001, ApJ, 557, 389
Uitenbroek, H. 2003, in ASP Conf. Ser. 286, Current Theoretical Models and Future High Resolution Solar Observations: Preparing for ATST, ed. A. A. Pevtsov & H. Uitenbroek (San Francisco, CA: ASP), 403
Vernazza, J. E., Avrett, E. H., & Loeser, R. 1981, ApJS, 45, 635
Wedemeyer, S., Bastian, T., Brajša, R., et al. 2016, SSRv, 200, 1
White, S. M., Iwai, K., Phillips, N. M., et al. 2017, SoPh, 292, 88
Wootten, A., & Thompson, A. R. 2009, IEEEP, 97, 1463
Yokoyama, T., Shimojo, M., Okamoto, T. J., & Iijima, H. 2018, ApJ, 863, 96